Planetary and Space Science 181 (2020) 104781

Contents lists available at ScienceDirect

Planetary and Space Science

journal homepage: www.elsevier.com/locate/pss

A mascon approach to estimating the depth of Jupiter's Great Red Spot with Juno gravity measurements

Marzia Parisi [a,*], William M. Folkner [a], Eli Galanti [b], Yohai Kaspi [b], Dustin R. Buccino [a], Kamal Oudrhiri [a], Scott J. Bolton [c]

[a] Jet Propulsion Laboratory, California Institute of Technology, Pasadena, CA, 91109, USA
[b] Department of Earth and Planetary Sciences, Weizmann Institute of Science, Rehovot, 76100, Israel
[c] Southwest Research Institute, San Antonio, TX, 78238, USA

ARTICLE INFO

Keywords:
Great red spot
Juno
Gravity science
Jupiter
Atmospheric dynamics
Orbit determination

ABSTRACT

We evaluate a method for determining the depth of Jupiter's Great Red Spot (GRS) with two *Juno* overflights dedicated to gravity science. The small-scale, localized nature of the anticyclone requires a detection method where the gravity perturbations are regional. To this end, we model the GRS as a dipole of flat disk mass concentrations (mascons), separated along the radial direction of Jupiter. Thermal wind theory predicts such structure composed of two equal and opposite masses below the visible cloud tops, condition that is used to constrain our estimation algorithm. Furthermore, Juno radiometer observations of the GRS brightness temperature indicate the presence of anomalies of opposite sign at different depths. We present the results of both a covariance and recovery analyses of the simulated data, in terms of accuracy in the estimation of the GRS mass and depth of winds. The analyses are carried out using precise Doppler tracking of the Juno spacecraft and by posing constraints on the interior model of the vortex from theory. We find that, if the surface dynamics extend at least several hundred kilometers below the cloud tops, it is possible to resolve the mass concentrations using both gravity passes, and tie the mass to the vortex's depth through thermal wind.

1. Introduction

The Great Red Spot (GRS) is an outstanding feature of Jupiter's atmosphere and the target of extensive observations since the late 1800s. The vortex is embedded in the strong Jovian zonal jets, and drifts with respect to the uniform rotation (System III). The physical appearance and characteristics of the anticyclonic storm are continuously changing, with recent observations concluding that its transition from elliptical to circular shape is progressing with an approximately linear trend (Simon et al., 2018). The Juno mission enabled considerable advances in the study of the GRS rich dynamics (Sànchez-Lavega et al., 2018), however the question concerning the depth of the vortex still stands. On a larger scale, it has been long debated whether Jupiter's strong zonal winds that are visible at the cloud level are shallow or deep (Busse, 1976; Ingersoll and Pollard, 1982; Vasavada and Showman, 2005). Juno provided an answer to this long-standing question by measuring the asymmetric gravity field of the planet (Iess et al., 2018), and concluded that the zonal winds must extend a few thousand kilometers below the cloud level to explain the measured odd gravity signal (Kaspi et al., 2018). It is still unknown whether the GRS is as deep as the zonal winds or characterized by a different scale height. It has been argued that the vortex is shallow and constrained to a thin weather layer despite its long lifespan (Dowling and Ingersoll, 1988; Morales-Juberias and Dowling, 2013). Others have argued that the vortex longevity can only be explained by deep roots extending into the interiors (Yano and Flierl, 1994). The first Juno overflight of the GRS occurred on 11 July 2017 (labeled as PJ07, short for perijove 7) and was optimized for Microwave Radiometer (MWR) observations, which measured the vortex's thermal emission, penetrating down to a few hundred bars, about 350 km below the 1-bar reference surface. The instrument observed colder than average brightness temperature anomalies in the upper levels and warmer anomalies at depth, indicating a sign inversion of the temperature perturbation (Li et al., 2017), which is akin to a dipole structure. What happens below a few hundred kilometers is still a mystery.

The Juno science orbits over the GRS, scheduled for February (PJ18) and July 2019 (PJ21), provide the opportunity to observe the storm and provide constraints on its depth. The two passes are dedicated to gravity science, the high-gain antenna (HGA) is Earth-pointed and provides a

* Corresponding author.
E-mail address: marzia.parisi@jpl.nasa.gov (M. Parisi).

https://doi.org/10.1016/j.pss.2019.104781
Received 22 February 2019; Received in revised form 15 October 2019; Accepted 18 October 2019
Available online 23 October 2019
0032-0633/

high signal-to-noise ratio. The detection of the GRS gravity signal using Juno data was proposed by Parisi et al. (2016), whose analysis considered a single close flyby of the GRS. The method relied on spherical harmonics, as the GRS makes up for a large part of the predicted non-axially symmetric gravity field. They concluded that the gravity signal of the GRS could be detected with a single overflight only if the vortex was deeper than 2000 km, since a 30×30 tesseral field was needed to define accurately the GRS gravity signal. In the present work, we resort to a different model to describe the concentrated mass anomalies expected from the vortex circulation. Mascons are mass concentrations that were first defined in Muller & Sjogren (Muller and Sjogren, 1968). They can assume different shapes and their use is particularly apt for solid bodies, for instance they have been used for the analysis of gravity data from the GRACE (Jacob et al., 2012) and GRAIL (Zuber et al., 2013) missions. In 1976, Null (1976) attempted to estimate the mass concentration of the GRS with *Pioneer* 10 and 11 radiometric data. He adopted a single mascon model and by combining the two encounters with Jupiter he concluded that the effect of the vortex on range-rate measurements was negligible at such distances (2.8 and 1.6 Jupiter radii, respectively). In 2019, Juno is scheduled to fly twice over the GRS within 1.3 Jupiter radii, opening up the possibility for the detection of its anomaly with gravity measurements, and define its deep structure. The purpose of this work is to link the estimation of the mascon masses, accompanied by the expected accuracies, to the vortex's depth. The objective is achieved by means of a covariance analysis and a partial recovery analysis, where the GRS mass is perturbed.

This paper is structured as follows. In Section 2 we introduce the thermal wind model, used to relate Jupiter's turbolent surface winds around the GRS to the expected gravity anomalies. In Section 3 we define a model of the vortex which features a dipole of disk mascons and the relationships between its properties. In Section 4 we report the results of the covariance and recovery analyses in terms of formal uncertainties in the estimation of the GRS mass anomalies. In Section 5 we present our conclusions and discuss the validity and limitations of our method for the determination of the GRS depth with Juno gravity data.

2. The wind-gravity relation

The thermal wind (TW) equation has been widely used in the past to explain Jupiter's large-scale dynamics (Kaspi et al., 2009; Kaspi et al., 2010) and the gravity field derived from the density anomaly profile has matched with remarkable accuracy the values of the first four odd harmonics of Jupiter's gravity field (Kaspi et al., 2018). Kaspi et al. (2018) were able to invert the observed asymmetric gravity field into a wind field by using an optimization based on the adjoint method (Galanti et al., 2017b). Similarly, assuming that, to first order, the dynamics of the GRS are geostrophic, the TW model can be used to predict the density anomalies associated with the strong anticyclonic flow (Parisi et al., 2016). The atmosphere of Jupiter is rotating differentially with surface velocities that are known from multi-spectral observations of the atmosphere during the *Cassini* Jupiter flyby in December 2000 (Choi and Showman, 2011). Fig. 1a shows the magnitude of the wind speed around the GRS location, within an area of 24° in latitude and 34° in longitude, after removing the zonal average from Equation (1), to highlight the azimuthal variations of the winds characteristic of the GRS (Parisi et al., 2016). The velocities of the vortex walls reach magnitudes of up to 90 ms^{-1} with respect to the background zonal flows (Choi and Showman, 2011). The north-south velocity profile is asymmetric with respect to latitude 20°S, with the northern edge of the collar characterized by higher wind speeds than the southern edge. The eastward longitude of the GRS geometric center in Jupiter System III was 274° in December 2000, at the time of the Cassini flyby. However, the GRS drifts westward relative to System III by about 0.36° per day (Simon et al., 2018).

Similar to Kaspi (2013), Parisi et al. (2016) and Kaspi et al. (2018), we propagate the surface velocity profile downwards along cylinders and assume an exponential decay in the radial direction by choosing the scale height H:

$$\begin{aligned} u(r,\theta,\varphi) &= u_{\mathrm{cyl}}(r,\theta,\varphi)e^{-\frac{R_J-r}{H}}, \\ v(r,\theta,\varphi) &= v_{\mathrm{cyl}}(r,\theta,\varphi)e^{-\frac{R_J-r}{H}}, \end{aligned} \tag{1}$$

where u is the azimuthal component of the velocity (east-west), v is the meridional component (north-south) and r, θ, φ are respectively the distance from the center of the planet, latitude and longitude in Jupiter System III. The functions $u_{\mathrm{cyl}}, v_{\mathrm{cyl}}$ are obtained by propagating the wind speed components, as measured at the cloud level (Choi and Showman, 2011), along the spin direction (Kaspi et al., 2009; Schneider and Liu, 2009). R_J is Jupiter's mean radius. Fig. 1b shows the wind speed as a function of depth, for $H = 300$ km, along the radial direction of Jupiter at a fixed longitude (274°E).

The TW equation relates the velocity profile of a fluid to density anomalies, assuming that the horizontal pressure gradients are balanced by the Coriolis force in the momentum conservation. This assumption is valid for Jupiter, as the Rossby number is small because of its fast rotation and large scales (Pedlosky, 1987). The equation is (Kaspi et al., 2009):

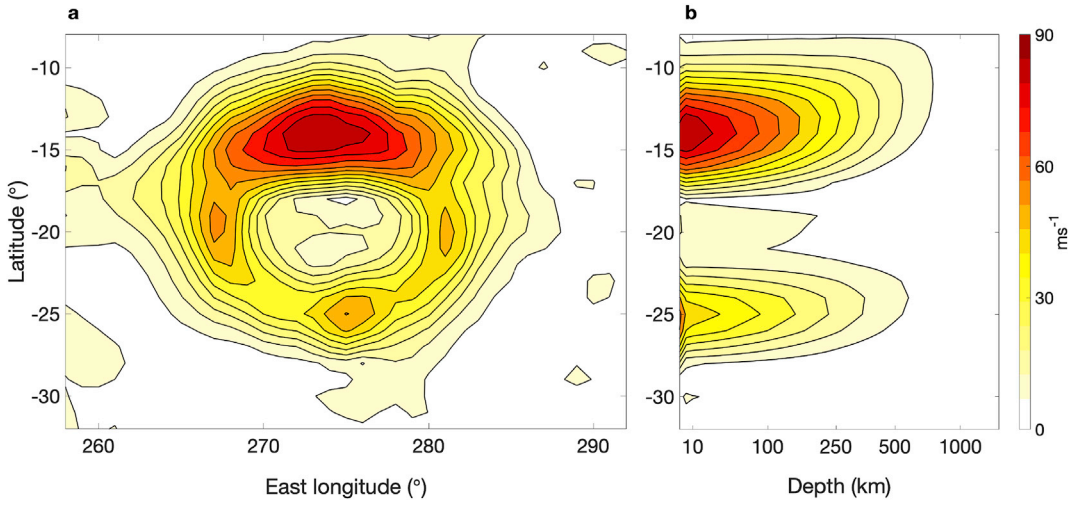

Fig. 1. Panel a: magnitude of the GRS velocity at the cloud level in Jupiter System III (in ms^{-1}), as seen by Cassini in the year 2000 (Choi and Showman, 2011). The winds that constitute the external walls of the GRS are rotating anticlockwise. Panel b: magnitude of the GRS winds as a function of depth, for $H = 300$ km. Vertical section along the GRS longitude at the time of the Cassini flyby (274°E).

$$2\boldsymbol{\Omega}\cdot\nabla(\tilde{\rho}\boldsymbol{v}) = \nabla\rho' \times \boldsymbol{g}, \quad (2)$$

where $\boldsymbol{\Omega}$ is Jupiter's mean rotation rate (corresponding to a period of ≈ 9 h 55 m 30s), $\boldsymbol{v}$ is the velocity vector and $\boldsymbol{g}$ is the radial gravity vector. The density is composed of a static component $\tilde{\rho}(r)$ and small anomalies related to the dynamics $\rho'(r,\theta,\varphi)$. The latter are linked to the dynamics of the atmosphere and are much smaller than the former. In this analysis we assume that the effect of the oblateness of the planet in Equation (2) is negligible, since this contribution is of second order in the description of the large-scale dynamics of Jupiter (Galanti et al., 2017a).

3. The Great Red Spot dipole model

3.1. Density profile

Equation (2) is broken into a system of scalar differential equations and solved numerically for ρ' over a horizontal grid of 180°(lat) x360°(long) and 87 non-equally spaced vertical levels (depth), given the wind profile in Equation (1) and the radial gravity vector (Parisi et al., 2016). The structure of the density perturbations at the GRS location (called henceforth Finite Element model) is revealed by showing a vertical section of the planet at longitude 274°E (Fig. 2a and b) and for a limited range of latitudes around the vortex's center. For $H = 300$ km (a) the density anomaly reaches a maximum positive value of 0.016 kgm^{-3} at a depth of 260 km, while changing sign and reaching a maximum negative value of −0.006 kgm^{-3} at 1000 km depth. For $H = 1000$ km (b), the peak values of the density contrast are 0.050 kgm^{-3} and −0.020 kgm^{-3} at depths of 800 km and 2400 km respectively. In both cases, the GRS density anomalies are structured as a dipole in the radial direction, positive closer to the cloud top and negative at depth. The anti-cyclonic circulation causes a mass up-welling at higher altitudes, and a mass deficiency at depth. The density profile obtained by integrating the TW equation is defined short of a constant of integration which is a function of the radial distance r. The constant can assume different values at different radial levels and produce different density profiles from the ones in Fig. 2. However, the Juno Doppler data are sensitive to variations in the mass density along its flight path with respect to the background density. In view of this, if we consider the density gradient on each horizontal level, its profile as a function of depth is independent of the constant of integration. To understand the physics behind the dipole structure we must consider the radial derivative ($\frac{\partial}{\partial r}$) of the term $\nabla(\tilde{\rho}\boldsymbol{v})$ in Equation (2). While the hydrostatic density increases with depth, the velocity decreases exponentially along the radial direction. These opposite effects are responsible for the change of sign in the density anomaly ρ'. Specifically, the background density gradient sets the overall positive radial gradient in the upper levels of the atmosphere, while the negative wind gradient dominates at depth.

The vertical mass dipole structure is also supported by Juno MWR observations of the GRS deep structure, obtained by measuring the thermal emission from Jupiter's atmosphere down to a few hundred bars. The shallower layers (closer to the surface) show colder than the background temperature anomalies, whereas the deepest layers show warmer than the background anomalies (Li et al., 2017). The structure and magnitude of the brightness temperature suggest a sign inversion of the observed anomaly, which is consistent with a dipole where the density anomaly changes sign accordingly, with denser fluid closer to the surface and less dense at depth. Since the temperature sign shift appears to take place within 350 km of the visible clouds, we focus our simulation efforts on scale heights shorter than 1000 km.

3.2. Relationship between dipole mass, scale height and radial distance

The mass anomaly per unit length associated with the GRS and function of the coordinate r (depth), is obtained by integrating the density anomaly profile (*e.g.* Fig. 2a and b) over the horizontal coordinates (θ and φ) for each vertical level. The positive mass anomaly GM_A is calculated by integrating the mass per unit length from the surface until the density anomaly changes sign. The negative mass anomaly GM_B is equal

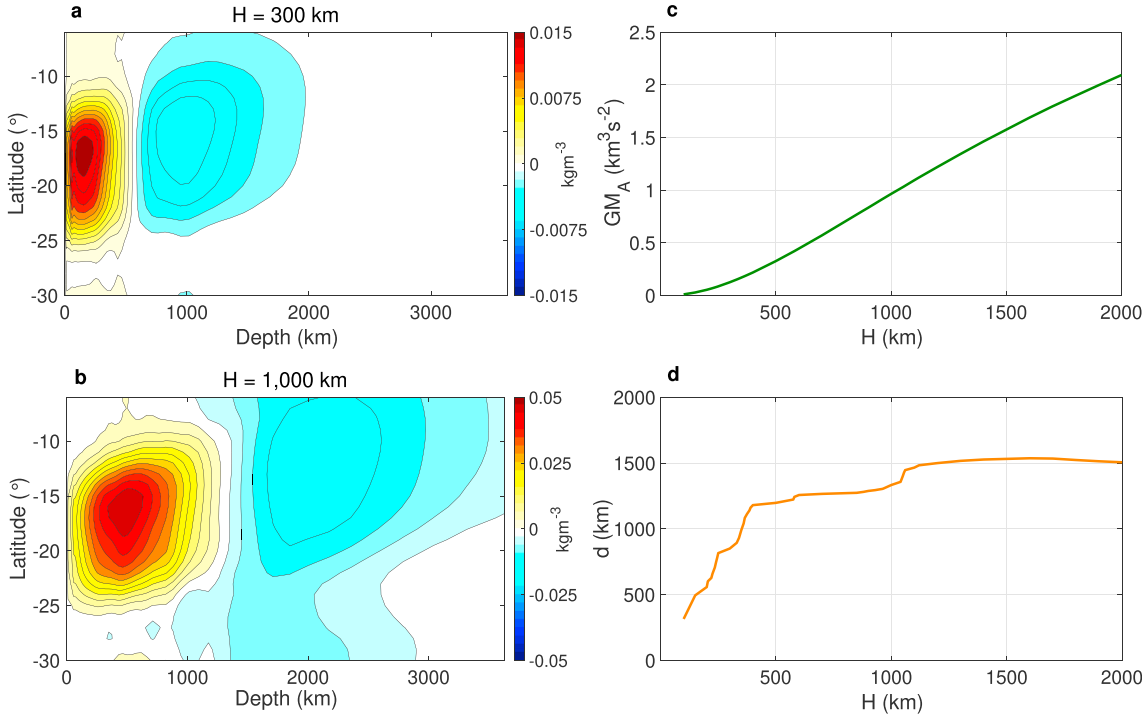

Fig. 2. Panels a and b: density anomalies at the GRS location and for different vertical levels, derived from the TW equation. The profiles are functions of depth and latitude, for a wind scale height of 300 km (a) and 1000 km (b). The density profiles can be compared to mass dipoles featuring a positive density anomaly close to the surface and a negative density anomaly at depth. Panel c: mass anomaly GM_A associated with the mass concentrations constituting the GRS, as a function of the scale height H. Panel d: vertical distance d between the positive and negative mass anomalies, as a function of the scale height H.

and opposite ($GM_A = -GM_B$). The latter constraint is a consequence of assuming mass conservation in the derivation of Equation (2). However, mass balance is applied over the entire spherical domain (Jupiter's mass is kept constant), and conservation locally and specifically along the radial coordinate is not guaranteed. Nevertheless, we find that the model maintains mass balance also in sub-domains if certain conditions are satisfied. We find that the constraint ($GM_A = -GM_B$) is best satisfied for shorter scale heights ($H < 1500$ km), whereas deeper GRS models show a residual mass, defined as $|(GM_A + GM_B)/GM_A|$ between 5 and 20%. The growing difference between the two masses is linked to the balance between the gradient of the hydrostatic density and the wind velocity for deeper models. In conclusion, for scale heights considered in this analysis (300–1000 km), mass conservation is satisfied. Fig. 2c shows the GRS positive mass anomaly (GM_A) as a function of the scale height H. In relation to our examples, the mass parameter amounts to about 0.126 km^3s^{-2} for $H = 300$ km and 0.965 km^3s^{-2} for $H = 1000$ km. For scale heights less than 1000 km the mass increases more than linearly with H, whereas for larger values the trend is less than linear. The plot shows the unique relationship between the mass involved in the GRS dynamics and its depth, hence the determination of the constrained positive and negative masses entails the estimation of its scale height.

The positive and negative masses are separated by a physical radial distance denoted hereafter as d. The parameter d is different from the scale height H, which represents instead the e-folding factor of the surface velocity profile. The relationship between H and d is unique and is shown in Fig. 2d. For H smaller than 1500 km, the radial distance d is larger than H, while beyond this value, it remains almost constant. Specifically to our sample cases, the radial separation is about 740 km for a dipole of scale height 300 km and 1600 km for a dipole of scale height 1000 km. Since d is small compared to the planet's radius (less than 2.5% of Jupiter's radius in the cases considered in the study) and the mascon masses are equal but opposite, to first order approximation we can assume that the position of Jupiter's center of mass does not shift.

In this subsection we have introduced three parameters that define the mass anomalies associated with the Great Red Spot: the wind scale height H, the mass anomaly GM_A and the vertical distance d. Fig. 2c and d shows that these parameters are tied to each other by unique relationships, and the dipole model is described by only one independent parameter.

3.3. The dipole model in the orbit determination software

Following the results from the integration of the TW equation, the GRS is modeled in the orbit determination software as a pair of flat disk mascons of radius R and separated by a radial distance d (Fig. 3). The positive disk mascon (A) lies close to the surface at the GRS location. Its depth relative to the reference ellipsoid is equal to the depth of the center of mass of the positive mass anomaly and depends on the scale height (Fig. 2a and b). Therefore d is a measure of the relative distance between the two mascons, and does not refer to the absolute depth below the visible clouds. The negative disk mascon (B) is located at the same longitude and latitude, but at a relative depth d with respect to A. The two mascons are constrained to have the same mass and opposite sign: $GM_A = -GM_B$. The radius of the disks is $R = 8000$ km, so that the circular area of the GRS is similar to the recently observed one (Simon et al., 2018; Sànchez-Lavega et al., 2018).

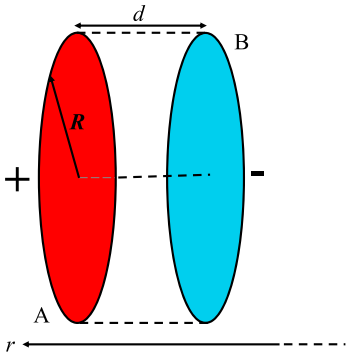

Fig. 3. Sketch of the GRS model in the orbit determination code. The pair of disk mascons (A and B) is characterized by the radius R, the masses GM_A and GM_B, and are separated radially by d. The Jovian radial coordinate r points outwards from the center of the planet.

From an orbit determination point of view, the GRS mass anomalies can be modeled using different approaches. For instance one could use a single mascon as in Null (1976), two or more mass concentrations located at different latitudes, spherical harmonics (Parisi et al., 2016) or Slepian functions (Galanti et al., 2019). All options are viable and might lead to the detection of the GRS gravity signal. However, in order to infer the depth of the GRS by determining its mass, it is necessary to make assumptions on the density distribution below the visible cloud tops. The choice to model the GRS density anomalies as a pair of concentrated masses at different altitudes is primarily based on the TW equation which can be used to predict the density distribution starting from wind profiles (Fig. 2a and b), as demonstrated in Kaspi et al. (2018) and Iess et al. (2019); and on Juno MWR observations of brightness temperature anomalies, which undergo a sign inversion as a function of depth (Li et al., 2017). Generally speaking, measurements of the gravity field of planetary bodies are afflicted by non-uniqueness, since a variety of density profiles can fit the same measurements. Yet, we can rely on physical consideration and detailed theoretical models to choose among the space of possible solutions.

In Fig. 4 we compare the gravitational potential of the GRS along the Juno trajectory for different models of the vortex and during a sample close overflight. The models are: i) the Finite Element (FE) model of the density anomalies as shown in Fig. 2a ($H = 300$ km), by considering each element of the three-dimensional grid as a point mass (solid green line). This represents the reference model that we aim to approximate. ii) The vertical dipole model (as in Fig. 3) using disk mascons stacked on top of each other (blue dotted line), from the mathematical formulation in Lass

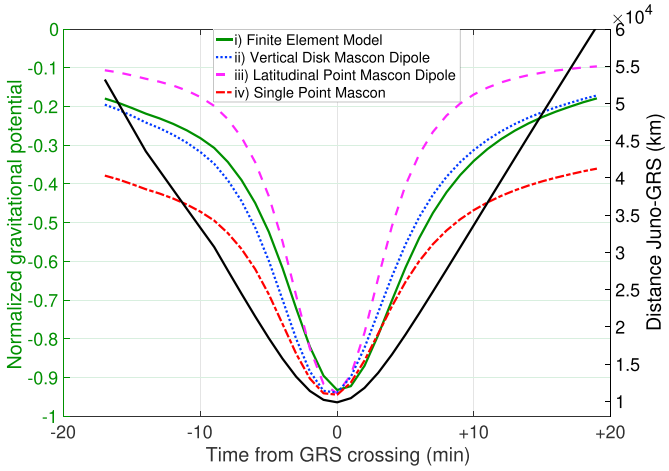

Fig. 4. Left y-axis: normalized gravitational potential of the GRS for $H = 300$ km, as a function of time, for four models: i) the Finite Element model (solid green line), from the integration of the TW equation; ii) a dipole (blue dotted line) composed of two disk mascons separated by a radial distance d (as in Fig. 3); iii) two mascons at different latitudes (10°S and 25°S) at an intermediate depth between the positive and negative mass anomalies of the TW density distribution (pink dashed line); iv) one point mass concentration at an intermediate depth between the positive and negative mass anomalies of the TW density distribution (red dashed line). Right y-axis: distance r' between the Juno spacecraft and the GRS during a close overflight (solid black line) as a function of time. (For interpretation of the references to colour in this figure legend, the reader is referred to the Web version of this article.)

& Blitzer (Lass and Blitzer, 1982), the vertical distance d is inferred from Fig. 2c at $H = 300$ km iii) Two point mass concentrations at different latitudes (10°S and 25°S) at an intermediate depth between the two mass anomalies of model (i) (pink dashed line). iv) A single point mass concentration (red dashed line) at an intermediate depth between the two mass anomalies of model (i). We find that the vertical dipole model (ii) approximates the reference TW model (i) in the most accurate way. Both potentials follow a similar power law of the distance r' between the spacecraft and the GRS. When sufficiently distant from the dipole, the potential varies like $(r')^{-2}$, whereas when closer to the concentrated masses, the spacecraft senses the closer positive mass and the power law is closer to $(r')^{-1}$. The potential from the FE model is slightly asymmetrical with respect to the time of closest approach between the spacecraft and the center of the GRS, which reflects the slight asymmetry with respect to latitude 20°S in the density distribution (Fig. 2a and b). The northward shift of the negative mascon is due to the alignment of u_{cyl} and v_{cyl} with the spin axis, which is neglected in this analysis, as the vertical dipole (ii) is still a good approximation of the density distribution (i) obtained from the integration of Equation (2). In reference to the vertical dipole model, as the scale height increases beyond 1000 km, the spacecraft becomes more sensitive to the acceleration from the positive mass closer to the surface, whereas the signal from the negative mass concentration is no longer detectable and blurs into the background. The gravitational potential differs from that exerted by a dipole and is closer to a gravitational monopole. This effect suggests the presence of a maximum detectable value of H, however this limit is well beyond the scale height range considered in this study (300–1000 km).

In the simulations we assumed the same circular shape and radius for the positive and negative disk mascons. In reality, the concentrated masses arising from the GRS circulation might deviate from this condition. We have analyzed the subtle changes in the gravitational potential of dipoles with masses varying in shape and size. We conclude that, as long as the mascon masses are equal and opposite, the dipole sketched in Fig. 3 remains a good approximation of the Finite Element model, regardless of the shape and size of the concentrations A and B.

3.4. Estimation strategy

In subsections 3.2 and 3.3 we deduced that the GRS dipole model is described by one independent parameter only. Eventually, the real overflight data will be combined in a square-root information filter and the recovery strategy will rely on the estimation of a single parameter related to the GRS, and on updating the dynamical model accordingly. The chosen estimated parameter is the mass of the positive mascon (GM_A), whereas the mass of the negative anomaly is constrained, in the filter, to be equal and opposite. At iteration zero, we select an initial value for the mascon mass GM_{AI}. To the initial mass corresponds set values of the scale height H_I and vertical distance d_I (from Fig. 2c and d). However, the initial guess for the mascon mass will likely be different from the truth. When the Doppler data is processed, adjustments to the mascon masses are estimated. From that it is possible to derive a new scale height (Fig. 2c), from which also the distance d between the mascons is determined (Fig. 2d). This leads to a new definition of the dipole in the dynamical model, which is used to re-analyze the Doppler data. The first iteration will make a new adjustment to the masses, from which new values for H and d can be derived. The process is repeated until convergence. The new estimation of the mascon mass will not only update the value of the mass itself, but will also change the partial derivatives of the parameters of interest and the covariance matrix at each iteration. This represents a limitation of our method which can result in a slower convergence of the estimation method and can be addressed by performing a larger number of iterations to test the stability of the solution.

In the next section we describe how this strategy is applied to the case of the Juno overflights of the Great Red Spot.

4. Detectability of the GRS with Juno gravity orbits

The Juno spacecraft was inserted in a highly eccentric, quasi-polar orbit around Jupiter in the summer of 2016. The closest approaches to the planet, or perijoves, occur roughly every 53 days (the orbital period). During the overflights, the spacecraft flies over Jupiter's cloud tops down to altitudes as low as 4000 km. The spacecraft has a limited amount of time to collect data at periapsis, therefore the science orbits have to be optimized for different instruments in order to maximize the scientific return of the mission. The objective of this work is determining whether it is possible to detect the GRS gravity signal with two targeted Juno gravity passes, using the vertical dipole model in Fig. 3. We simulated two-way Doppler data for PJ18 and PJ21, which will use both X- and Ka-band links (7.2–8.4 GHz and 32.5–34 GHz), received and transmitted through the onboard High Gain Antenna (HGA). The Juno spacecraft will fly over the GRS at an altitude of about 13,000 km during PJ18, and slightly over 19,000 km during PJ21. The longitudinal offset between the spacecraft and the GRS will be about 10° and 6°, respectively (Fig. 5). In addition to the two critical overflights of the GRS, we simulated data for Juno perijoves that were (or, for future ones, that will, tentatively, be) optimized for gravity measurements: PJ03, PJ06, PJ08, PJ10, PJ11, PJ14, PJ15, PJ17, PJ22, PJ23 and PJ25-PJ33. Although only PJ18 and PJ21 will physically fly over the GRS, including the rest of the gravity passes helps constraining the global gravity field of the planet and the spacecraft state at the beginning of each arc, which ultimately affect the determination of the GRS mass. The noise level used to simulate the Doppler data, which is a linear combination of X- and Ka-band for plasma noise cancellation, was chosen as follows. For perijoves already occurred at the time of our simulations (PJ1 to PJ17), we adopted actual data weights used in the gravity data analysis, between 5 and 10 μms^{-1} (one-way) for an integration time of 60 s. For instance, PJ03 and PJ06 one-way noise level was about 7.5 μms^{-1} (Iess et al., 2018). For future perijoves we used data weights ranging between 8 and 10 μms^{-1} (one-way, 60 s). The noise root mean square (RMS) of Doppler measurements for each

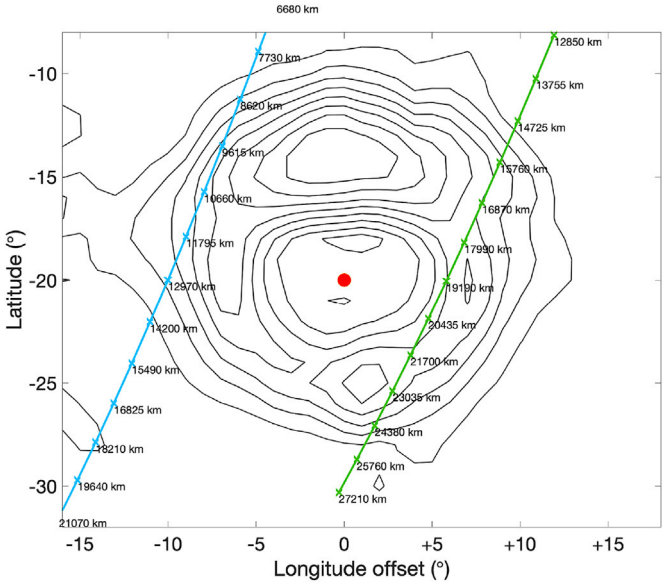

Fig. 5. Predicted ground tracks for PJ18 (blue line) and PJ21 (green line) with respect to the GRS expected location (red dot). The contour plot is used to define the GRS area, and uses the wind speed profile from (Choi & Showman 6). One has to remember that the shape and size of the vortex is continuously changing, (Simon et al., 2018). The altitude of the Juno spacecraft while flying over the GRS is marked (in km) along the tracks. The predicted longitude offset and overflight altitude are about −10° and 13,000 km for PJ18, and +6° and 19,000 km for PJ21. (For interpretation of the references to colour in this figure legend, the reader is referred to the Web version of this article.)

perijove depends on several factors. The employment of two independent radio carriers is used to calibrate up to 75% of dispersive noise (Bertotti et al., 1993), due to Earth's ionosphere, solar plasma and, specifically for Juno, the Io Plasma Torus (Phipps et al., 2018, 2019). The noise caused by the wet component of Earth's troposphere is accurately calibrated using water vapor radiometers located near the ground antenna (Iess et al., 2018).

4.1. The dynamical model

In order to integrate the trajectory of Juno and simulate the radiometric data, we defined a dynamical model to describe the forces acting on the spacecraft, in addition to the GRS mascons already discussed in Section 3. The model included: Jupiter's point mass acceleration from the Jet Propulsion Laboratory (JPL) planetary ephemeris DE438 (Folkner, 2019), along with the Sun and the other planets; Jupiter's spin axis position from the latest IAU model (Archinal et al., 2010); zonal harmonic coefficients from degree 2 to 50, the nominal values for J_2-J_{12} were taken from Iess et al. (2018), whereas for higher degrees the nominal value is set to zero; tidal deformations caused by the Galilean satellites up to degree 6, according to Wahl et al. (2016). Other notable accelerations are the point mass accelerations from the main satellites as reported in JPL's satellite ephemeris JUP310 (Jacobson, 2019); solar pressure, Jupiter's albedo and thermal emission, which require information about the spacecraft structure. The solar panels represent the dominant feature, with a total area of about 60 m^2, while the whole spacecraft is spinning at 2 rpm during science operations (Bolton et al., 2017a).

Simulated Doppler data at 60 s integration time from all perijoves are combined in a multiarc square-root information filter to estimate parameters of interest. Each element of the solve-for vector influences the recovery of the GRS mascon masses and will be discussed in the following paragraphs. The chosen set of estimated parameters for the numerical simulations is: Jupiter's mass parameter (GM) with an *a priori* uncertainty of 2 km^3s^{-2}; pole right ascension and declination (constant term and rate) with loosened *a priori* uncertainties; the precession rate with loosened *a priori* uncertainty; zonal harmonic coefficients J_2-J_{50} with loosened *a priori* uncertainties; 4×4 tesseral field coefficients with loosened *a priori* uncertainties; the state of the Juno spacecraft at the beginning of each gravity pass with *a priori* uncertainties of 10^9 km for the position and 1 kms^{-1} for the velocity; the tidal Love numbers $k_{m,n}$ when $m+n$ is an even number (up to degree-6), with *a priori* uncertainties of 1, for reference the expected value for k_{22} is close to 0.59 (Wahl et al., 2016). In addition, we estimate the masses of the two GRS mascons, GM_A and GM_B, with *a priori* uncertainties of 10^2 km^3s^{-2} and the constraint of being equal and opposite, as suggested by the TW model (see Section 3). The latter condition implies that the correlation coefficient between GM_A and GM_B is imposed to be -1. The filter is used to estimate the mass of one of the mascons while the mass of the opposite concentration is forced to be complementary. Furthermore, the Love numbers $k_{m,n}$ when $m+n$ is an odd number (up to degree-6) are not estimated but included as consider parameters (Tapley et al., 2004), implying that their *a priori* uncertainties (set to 1) and their correlations with the solve-for parameters are taken into account in the definition of the post-fit covariance matrix, but the data strength necessary to estimate them is not available. For a more detailed description of the Jupiter gravity field estimation with Juno see Bolton et al. (2017b), Folkner et al. (2017) and Iess et al. (2018).

4.2. Results of the covariance analysis

We will first discuss the outcome of the covariance analysis, where the dynamical model used to simulate the Doppler observables along the trajectory of each arc (described in the previous paragraphs) is the same as the one used to calculate the computed Doppler. The differences (residuals) between the simulated observed Doppler and computed Doppler will only show the simulated white noise. The objective is to study the covariance matrix, which contains information about the formal uncertainties on the estimated parameters and depends on the variability of the Doppler observable with each parameter. Rows labeled as COV in Table 1 show the expected formal uncertainty (σ_{GM_A}, 1-sigma) in the estimation of the mascons' masses, GM_A and GM_B for two different simulated values of H. The relative accuracy ($\sigma^{rel}_{GM_A}$) achieved with PJ18 alone is 59.5% of the expected mass variation for $H = 300$ km ($GM_A = 0.126$ km^3s^{-2}), ruling out the possibility of detecting a shallow GRS with a single flyby, since the estimated mascon mass is compatible with zero well within the 3-sigma level. The detectability improves by adding simulated gravity data from PJ21, with a smaller relative uncertainty (ratio between σ_{GM_A} and GM_A) of 42.9%. If the GRS is deep ($H = 1000$ km, $GM_A = 0.965$ km3s^{-2}), the relative uncertainty is reduced to 5.2% and 3.8% with one and two overflights, respectively. The standard deviation depends on the scale height of the dipole model, specifically, dipoles characterized by a larger radial separation are better resolved in the gravity solution. This can be explained by the increase in the mass involved in the vortex circulation (Fig. 2c). A second-order effect is the larger radial separation (Fig. 2d), where the two opposite masses cancel each other less when further apart. Both effects produce a larger dipole moment, which is the product between GM_A and d. The results of the covariance analysis suggest that the minimum detectable scale height for the GRS is larger than 300 but well below 1000 km.

The estimation accuracies of the remaining gravity coefficients are not discussed, however we will discuss their influence on the estimation of the dipole masses. The correlation coefficients of the mascon mass parameter with the other components of the estimated vector are below 0.60. The highest correlations with gravity parameters are found with the Love numbers, with a peak of 0.46 for degree-2 coefficients. Since the maximum detectable degree (5) for the Love numbers is already included in the covariance matrix, we study instead the effect of estimating a higher degree tesseral field on the formal uncertainties of the mascon masses. We find that estimating a 5×5 or 6×6 tesseral field degrades the relative uncertainties in Table 1 by less than 5%, pointing to low correlation coefficients with longitudinal variations of the gravity field. Correlations of the mascon parameters with the zonal gravity harmonics are low as well (< 0.1). Finally, we report that the estimation errors (differences between simulated and estimated values) are below the 3-sigma level for all the components of the solve-for vector. We find that the estimation of the mascon masses has no detectable influence on the estimation of the zonal coefficients of the gravity field, which depend on latitudinal variations of the field. The absolute and relative errors are listed for GM_A (ε_{GM_A} and $\varepsilon^{rel}_{GM_A}$, Table 1). The uncertainty on the scale height of the GRS in Table 1 (σ_H) is derived from the estimation of the mascon masses as:

$$\sigma_H^2 = \left(\frac{\partial H}{\partial GM_A}\right)^2 \sigma^2_{GM_A} \tag{3}$$

where $\frac{\partial H}{\partial GM_A}$ is the inverse of the derivative of the curve in Fig. 2c, calculated at the estimated GM_A. The smaller formal uncertainties on H for deeper cases is explained by the slope of the curve in Fig. 2c being steeper around 1000 km than around 300 km. However, since the curve becomes flatter after 1000 km, we expect the formal uncertainty on H to increase after this value.

4.3. Results of the recovery analysis

The vertical distance d that characterizes the GRS and is used in the dynamical model varies according to the estimated mass of the mascons and hence affects the formal uncertainty on GM_A. The independent estimation of both mass and vertical separation of the mascons requires greater data strength. However, using theoretical considerations these parameters are constrained by the TW model and one (*e.g.* d) can be inferred from the other (*e.g.* GM_A), as they are both functions of the scale height (Subsection 3.2). In order to explore the relationship between

Table 1
Simulation results of the estimation of the mascon mass (GM_A) and scale height (H) for the covariance (COV) and recovery (REC) analyses, considering one or two GRS overflights. The recovery analysis refers to the tests where the initial guess for the GRS mass is different from the simulated value. The table shows, in order: σ_{GM_A} is the formal uncertainty or 1-sigma uncertainty; $\sigma^{rel}_{GM_A}$ is the relative uncertainty (%) defined as the ratio between the formal uncertainty and the simulated value for GM_A; ε_{GM_A} is the estimation error (recovered value minus simulated value) on the mascon mass; $\varepsilon^{rel}_{GM_A}$ is the relative estimation error, defined as the ratio between the mass estimation error and the formal uncertainty (number of sigmas); σ_H is the formal uncertainty on the scale height H. All quantities are shown for the shallow ($H = 300$ km) and deep ($H = 1000$ km) cases.

GRS Perijove		σ_{GM_A} (km^3s^{-2})		$\sigma^{rel}_{GM_A}$ (%)		ε_{GM_A} (km^3s^{-2})		$\varepsilon^{rel}_{GM_A}$ (sigmas)		σ_H (km)	
		H_{300}	H_{1000}	H_{300}	H_{1000}	H_{300}	H_{1000}	H_{300}	H_{1000}	H_{300}	H_{1000}
COV	PJ18	0.075	0.050	59.5	5.2	0.064	0.077	0.9	1.5	105	40
	PJ18 & PJ21	0.054	0.037	42.9	3.8	0.004	0.074	0.1	2.0	70	30
REC	PJ18	0.090	0.052	71.4	5.4	0.114	0.026	1.3	0.5	135	45
	PJ18 & PJ21	0.057	0.034	45.2	3.5	0.030	0.098[a]	0.5	2.9[a]	75	35

[a] The estimation error for this case was obtained after three iterations. For all other cases the reported estimation errors were obtained after two iterations.

estimated mass and scale height, we performed a partial recovery analysis, where the simulated scale height for the GRS is different from the initial guess used to generate the computed observables (see process described in Subsection 3.4).

For instance, we simulated tracking data for PJ18 and PJ21 assuming a GRS scale height of 300 km, a mascon mass of 0.126 km^3s^{-2} and a radial separation of 740 km (inferred from Fig. 2c and d respectively). Our goal is to determine whether it is possible to recover the true value for the scale height, which can fit the simulated Doppler data to the noise level. We start from a first-guess scale height of 1000 km, a mascon mass of 0.965 km^3s^{-2} and a radial distance of 1600 km. Since these values are different from the simulated ones, unlike the covariance analysis, the Doppler residuals will now show dynamical signatures due to the slightly different accelerations exerted on the spacecraft by the different mascon models. At iteration 0, the new estimated value for the mascon masses is (0.122 ± 0.037) km^3s^{-2}, which corresponds to a smaller scale height of (295 ± 45) km, already closer to the simulated value. To retrieve the value and formal uncertainty on H from the estimated value of GM_A we used the plot in Fig. 2c and eq. (3). For the following iteration, we change accordingly the value of GM_A and d used in the dynamical model for the trajectory integration. After re-integrating the trajectory, the new estimate for the mascon masses is (0.234 ± 0.061) km^3s^{-2}, corresponding to a scale height of (415 ± 65) km. The recovered value of H oscillates around the simulated value and the process is repeated until the simulated Doppler data is fitted to the noise level and until the estimation error for the mascon GM_A is smaller than three times the formal uncertainty. After a small number of iterations (2), the converged estimate for the mascon mass is $\overline{GM_A} = (0.156 \pm 0.057)$ km^3s^{-2}, which corresponds to an estimated $\overline{H} = (330 \pm 75)$ km and is compatible at the 1-sigma level to the value used to simulate the data. The underlying assumption is that, whereas the location of the GRS varies in the dynamical model for PJ18 and PJ21 to match the predictions, its size, mass and overall structure remains constant throughout the simulation time (February–July 2019).

The analysis described in the previous paragraph can be repeated choosing different combinations of the simulated and first guess values for the GRS mass, considering only PJ18 or both PJ18 and PJ21. The results are reported in the rows labeled as REC in Table 1 and show that the formal and relative uncertainties on the estimated scale height are degraded by 30% at most in the single-flyby scenario and by 15% at most in the two-flyby scenario in comparison to the covariance analysis, due to their dependence on the scale height used in the dynamical model. After two iterations, the estimation errors in the recovery of the mascon masses are within the 3-sigma level, with the exception of the deep, PJ18 + PJ21 case, whose error is about four times the formal uncertainty. For this last case, the estimation error goes down to about 3 sigmas after the third iteration, and continues to decrease further after additional iterations. The slow convergence of the estimated mass is related to the strong interdependence between the value of the GRS scale height adopted in the dynamical model and the formal uncertainty, which changes the value of the partial derivatives for the mascon masses at each iteration.

We consider a simulated gravity solution as converged when the estimation error is, and continues to be after further iterations, below three times the formal uncertainty. Following this definition, in the previous paragraphs we have shown that convergence for GM_A is usually reached after two or three iterations for this set of simulations. Nonetheless, it is crucial to test the stability of the solution by monitoring the estimation error for a larger number of iterations (*e.g.* 15) and verify that this parameter remains under the three-sigma threshold for all estimated parameters.

5. Discussion and conclusion

In this work we describe a method for determining the depth of Jupiter's Great Red Spot with the Juno gravity experiment and by constraining its structure from thermal wind theory. The model captures the essential dipole-like structure of the vortex's density anomalies, with the advantage of using only one parameter to define it. This translates into a small number of coefficients to be estimated in the orbit determination process. Doppler data collected during the Juno overflights of the storm are very valuable and sophisticated calibration techniques must be employed in order to reduce the noise on radiometric observables. A smaller set of estimated parameters can make a crucial difference in the detection of the GRS gravity signal because of the limited available data strength (Parisi et al., 2016). Therefore, our ability to restrict the number of parameters associated with the GRS model is key to successfully determining its depth.

The effect of the GRS dipole on the Doppler residuals that has to be detected in order to infer its depth is very subtle and requires the removal of systematic errors due, for instance, to the ground and onboard instrumentation. Other small-scale effects, such as high-degree Jupiter's tides and tesseral field, must be included in the dynamical model in order to avoid aliasing of the estimated parameters, despite the correlations coefficients being small. In this analysis, systematic errors have not been included in the global fit and the initial Juno state and global gravity field of Jupiter have not been perturbed in the partial recovery analysis. Furthermore, uncertainties on the GRS drift rate might change the conditions of the upcoming overflights by changing the relative longitude between Juno and the GRS.

The results of our simulations show that the minimum detectable scale height is several hundred kilometers, provided that data from the two gravity overflights of the vortex are combined. The relative uncertainty on the mascon mass is between 42 and 45% for the 300 km case, below the detection threshold. For the very deep case ($H = 1000$ km), the relative uncertainties in the estimation of the mascon mass are conspicuously smaller, around 5%, well above the detection threshold. These results show a better detectability with a reduced minimum detection depth of the GRS, than what was found in Parisi et al. (2016), where only one single flyby of the Juno spacecraft was considered in the analysis and where the estimation of many parameters was required. Another limitation of the spherical harmonic approach is represented by the drift rate

that characterizes the GRS with respect to Jupiter System III. While the vortex moves in the body-fixed references frame, a detection using a tesseral gravity field requires the perturbations to be static, which is not the case when combining two overflights. On the other hand, the mascon approach allows us to account for the differential rotation of the vortex.

The recently published analysis by Galanti et al. (2019) presents an alternate method for the determination of the depth of the GRS based on Slepian functions, which are orthonormal functions defined over a latitudinally and longitudinally limited domain. The approach has points in common with this work, as both use the TW equation to predict the radial density distribution caused by the GRS circulation (Fig. 2a and b). In the Slepian approach the authors look at the surface gravity produced by the mass distribution, rather than at the density profile itself. The vertical mass dipole, which is amply described in this article, produces a north-south dipole in terms of surface gravity, with two gravity anomalies located at different latitudes (see Fig. 3 of Galanti et al., 2019). The authors also resort to describing the GRS gravitational signal with one parameter only, namely the coefficient of the second Slepian function (α_2) defined in a circular area centered at the GRS (see Fig. 2 of Galanti et al., 2019). The main result shown by Galanti et al. (2019) is that the depth of the GRS can be resolved with reasonable uncertainty if the GRS is deeper than 300 km, and that the uncertainty depends on the depth itself. The results shown in this article are slightly more pessimistic, as the minimum detectable depth for the GRS is determined to be somewhere between 300 and 1000 km. In the manuscript, Galanti et al. (2019) obtain a maximum detectable depth of 1800 km, whereas we suspect an upper limit of about 1500 km, although this number is not supported by simulations, only by theoretical considerations. The main limitation of the Slepian method is that the functions tend to lose orthogonality when gravity is sampled at a distance from the reference surface, which will be about 0.20 and 0.26 Jupiter's radii for PJ18 and PJ21 respectively. The authors address such issue in the manuscript by quantifying the level of degradation as a function of the spacecraft altitude and concluding that below 15,000 km the effect is negligible. The mascon method, compared to the Slepian approach, provides a direct estimation of TW parameters as opposed to estimating surface gravity and interpret it in terms of the GRS depth. The dipole intrinsically accounts for the correlations between the estimated parameters, which explains the slightly degraded, but perhaps more realistic, formal uncertainties.

The main limitations of the method presented in this paper are the heavy dependence on the assumed theoretical model (TW) and the changes in the mascon mass partial derivatives at every iteration, which may lead to slow convergence. If the actual density distribution around the GRS deviates significantly from TW, the results of a recovery analysis based on this method could be biased. However we don't expect this to be the case as TW theory was able to accurately match the Juno observations of Jupiter's asymmetric gravity field (Kaspi et al., 2018). Aliasing of the estimated parameters is always a possibility in orbit determination, especially when looking for a subtle effect such as the GRS gravity signature. In this paper we lay the foundation to answer a straightforward question about the vortex: is it very shallow or very deep? We are interested in determining the order of magnitude of the phenomenon. Intuitively, if the GRS is very deep, the mass involved in its circulation will be larger and the gravitational signature substantial. In other words, the local deviation from a purely zonal field (axially symmetric) during the Juno GRS overflights will be detectable if the anomaly extends for thousands of kilometers. Our method captures the basic mechanism of increasing mass anomalies for deeper flows (Fig. 2c) and allows to interpret the results in terms of depth of the GRS using TW theory.

In conclusion, both the mascon method described in this work and the Slepian approach by Galanti et al. (2019) are characterized by different advantages and limitations. The edge of using the former is the direct estimation of TW parameters, while using the latter guarantees a detection that is less model-dependent as it uses information about the surface gravity. The two detection techniques are meant to be used simultaneously once the real data are available, in order to provide a more robust answer in regard to the GRS depth, even more so if they can be combined with MWR observations.

Declaration of competing interest

None.

Acknowledgments

We thank the Juno Interior and Atmospheric Working Groups for the useful discussions. The research described in this paper was carried out at the Jet Propulsion Laboratory, California Institute of Technology, under a contract with the National Aeronautics and Space Administration (M.P., W.M.F., D.R.B. and K.O.); at the Weizmann Institute of Science in Israel (E.G. and Y.K.); at the Southwest Research Institute under a NASA contract (S.J.B.).

References

Archinal, B.A., A'Hearn, M.F., Bowell, E., Conrad, A., Consolmagno, G.J., Courtin, R., et al., 2010. Report of the IAU working group on cartographic coordinates and rotational elements: 2009. Celest. Mech. Dyn. Astron. 109 (2), 101–135.

Bertotti, B., Comoretto, G., Iess, L., 1993. Doppler tracking of spacecraft with multifrequency links. Astron. Astrophys. 269, 608–616.

Bolton, S.J., Lunine, J.I., Stevenson, D.J., Connerney, J.E.P., Levin, S.M., Owen, T.C., et al., 2017. The Juno mission. Space Sci. Rev. 213, 5–37. https://doi.org/10.1007/s11214-017-0429-6.

Bolton, S.J., Adriani, A., Adumitroaie, V., Allison, M., Anderson, J.D., Atreya, S., et al., 2017. Jupiter's interior and deep atmosphere: the initial pole-to-pole passes with the Juno spacecraft. Science 356 (6340), 821–825. https://doi.org/10.1126/science.aal2108.

Busse, F.H., 1976. A simple model of convection in the Jovian atmosphere. Icarus 29 (2), 255–260. https://doi.org/10.1016/0019-1035(76)90053-1.

Choi, D.S., Showman, A.P., 2011. Power spectral analysis of Jupiter's clouds and kinetic energy from Cassini. Icarus 216 (2), 597–609. https://doi.org/10.1016/j.icarus.2011.10.001.

Dowling, T.E., Ingersoll, A.P., 1988. Jupiter's Great red Spot as a shallow water system. J. Atmos. Sci. 46 (21), 3256–3278. https://doi.org/10.1175/1520-0469(1989)046<3256:JGRSAA>2.0.CO;2.

Folkner, W.M., Iess, L., Anderson, J.D., Asmar, S.W., Buccino, D.R., Durante, D., Feldman, M., et al., 2017. Jupiter gravity field estimated from the first two Juno orbits. Geophys. Res. Lett. 44 (10), 4694–4700. https://doi.org/10.1002/2017GL073140.

Folkner, W.M., 2019. DE438 release notes. https://naif.jpl.nasa.gov/pub/naif/JUNO/kernels/spk/de438s.bsp.lbl.

Galanti, E., Kaspi, Y., Tziperman, E., 2017. A full, self-consistent, treatment of thermal wind balance on fluid planets. J. Comput. Phys. 810, 175–195. https://doi.org/10.1017/jfm.2016.687.

Galanti, E., Durante, D., Finocchiaro, Iess L., Kaspi, Y., 2017. Estimating Jupiter's gravity field using Juno measurements, trajectory estimation analysis, and a flow model optimization. Astron. J. 154 (1) https://doi.org/10.3847/1538-3881/aa72db.

Galanti, E., Kaspi, Y., Simons, F.J., Durante, D., Parisi, M., Bolton, S.J., 2019. Determining the depth of Jupiter's Great red Spot with Juno: a slepian approach. Astrono. J. Lett. 874 (2) https://doi.org/10.3847/2041-8213/ab1086.

Iess, L., Folkner, W.M., Durante, D., Parisi, M., Kaspi, Y., Galanti, E., Guillot, T., et al., 2018. Measurement of Jupiter's asymmetric gravity field. Nature 555, 220–222. https://doi.org/10.1038/nature25776.

Iess, L., Militzer, B., Kaspi, Y., Nicholson, P., Durante, D., Racioppa, P., et al., 2019. Measurement and implications of Saturn's gravity field and ring mass. Science. https://doi.org/10.1126/science.aat2965. (Accessed 17 January 2019).

Ingersoll, A.P., Pollard, D., 1982. Motion in the interiors and atmospheres of Jupiter and Saturn: scale analysis, anelastic equations, barotropic stability criterion. Icarus 52 (1), 62–80. https://doi.org/10.1016/0019-1035(82)90169-5.

Jacob, T., Wahr, J., Pfeffer, W.T., Swenson, S., 2012. Recent contributions of glaciers and ice caps to sea level rise. Nature 482, 514–518. https://doi.org/10.1038/nature10847.

Jacobson, R.A., 2019. JUP310 Satellite Ephemeris File Release. https://naif.jpl.nasa.gov/pub/naif/generic_kernels/spk/satellites/jup310.cmt.

Kaspi, Y., Flierl, G.R., Showman, A.P., 2009. The deep wind structure of the giant planets: results from an anelastic general circulation model. Icarus 202 (2), 525–542. https://doi.org/10.1016/j.icarus.2009.03.026.

Kaspi, Y., Hubbard, W.B., Showman, A.P., Flierl, G.R., 2010. The gravitational signature of Jupiter's internal dynamics. Geophys. Res. Lett. 37 (1), L01204. https://doi.org/10.1029/2009GL041385.

Kaspi, Y., 2013. Inferring the depth of the zonal jets on Jupiter and Saturn from odd gravity harmonics. Geophys. Res. Lett. 40 (4), 676–680. https://doi.org/10.1029/2012GL053873.

Kaspi, Y., Galanti, E., Hubbard, W.B., Stevenson, D.J., Bolton, S.J., Iess, L., Guillot, T., et al., 2018. Jupiter's atmospheric jet-streams extend thousands of kilometers deep. Nature 555, 223–226. https://doi.org/10.1038/nature25793.

Lass, H., Blitzer, L., 1982. The gravitational potential due to uniform disks and rings. Celestial Mech. 30 (3), 225–228. https://doi.org/10.1007/BF01232189.
Li, C., Oyafuso, F.A., Brown, S.T., Atreya, S.K., Orton, G.S., Ingersoll, A.P., Janssen, M.A., 2017. How Deep Is Jupiter's Great Red Spot? Paper Presented at American Geophysical Union Fall Meeting 2017. American Geophysical Union, New Orleans, Louisiana, USA.
Morales-Juberias, R., Dowling, T.E., 2013. Jupiter's Great Red Spot: fine-scale matches of model vorticity patterns to prevailing cloud patterns. Icarus 225 (1), 216–227. https://doi.org/10.1016/j.icarus.2013.03.026.
Muller, P.M., Sjogren, W.L., 1968. Mascons: lunar mass concentrations. Science 161 (3842), 680–684. https://doi.org/10.1126/science.161.3842.680.
Null, G.W., 1976. Gravity field of Jupiter and its satellites from Pioneer 10 and Pioneer 11 tracking data. Astron. J. 81 (12), 1153–1161. https://doi.org/10.1086/111999.
Parisi, M., Galanti, E., Finocchiaro, S., Iess, L., Kaspi, Y., 2016. Probing the depth of Jupiter's Great red Spot with the Juno gravity experiment. Icarus 267, 232–242. https://doi.org/10.1016/j.icarus.2015.12.011.
Pedlosky, J., 1987. Fundamentals: the thermal wind. In: Geophysical Fluid Dynamics. Springer-Verlag, New York, Heidelberg, Berlin, pp. 42–43. https://doi.org/10.1007/978-1-4684-0071-7.
Phipps, P.H., Withers, P., Buccino, D.R., Yang, Y.-M., 2018. Distribution of plasma in the Io plasma torus as seen by radio occultation during *Juno* perijove 1. J. Geophys. Res. Space Phys. 123 (8), 6207–6222. https://doi.org/10.1029/2017JA025113.
Phipps, P.H., Withers, P., Buccino, D.R., Yang, Y.-M., Parisi, M., 2019. Variations in the density distribution of the Io plasma torus as seen by radio occultations on Juno Perijoves 3, 6, and 8. J. Geophys. Res. Space Phys. 124 https://doi.org/10.1029/2018JA026297.
Sànchez-Lavega, A., Hueso, R., Eichsätdt, G., Orton, G.S., Rogers, J., Hansen, C.J., Momary, T., et al., 2018. The rich dynamics of Jupiter's Great red Spot from JunoCam; Juno images. Astronaut. J. 156 (4) https://doi.org/10.3847/1538-3881/aada81.
Schneider, T., Liu, J., 2009. Formation of jets and equatorial superrotation on Jupiter. J. Atmos. Sci. 66, 579–601. https://doi.org/10.1175/2008JAS2798.1.
Simon, A.A., Tabataba-Vakili, F., Cosentino, R., Beebe, R.F., Wong, M.H., Orton, G.S., 2018. Historical and contemporary trends in the size, drift, and color of Jupiter's Great red Spot. Astronaut. J. 155 (4) https://doi.org/10.3847/1538-3881/aaae01.
Tapley, B.D., Schutz, B.E., Born, G.H., 2004. Consider Covariance Analysis in Statistical Orbit Determination. Elsevier Inc., San Diego, CA, USA.
Vasavada, A.R., Showman, A.P., 2005. Jovian atmospheric dynamics: an update after Galileo and Cassini. Rep. Prog. Phys. 68 (8), 1935–1996. https://doi.org/10.1088/0034-4885/68/8/R06.
Wahl, S.M., Hubbard, W.B., Militzer, B., 2016. Tidal response of preliminary Jupiter model. Astrophys. J. 831 (14). https://doi:10.3847/0004-637X/831/1/14.
Yano, J., Flierl, G.R., 1994. Jupiter's Great Red Spot: compactness condition and stability. Ann. Geophys. 12 (1), 1–18. https://doi.org/10.1007/s00585-994-0001-z.
Zuber, M.T., Smith, D.E., Watkins, M.M., Asmar, S.W., Konopliv, A.S., Lemoine, F.G., Melosh, H.J., Neumann, G.A., Phillips, R.J., Solomon, S.C., Wieczorek, M.A., Williams, J.G., Goossens, S.J., Kruizinga, G., Mazarico, E., Park, R.S., Yuan, D.-N., 2013. Gravity field of the moon from the gravity recovery and interior laboratory (GRAIL) mission. Science 339 (6120), 668–671. https://doi.org/10.1126/science.1231507.